Topological Hall effect in weakly canted antiferromagnets

Jotaro J. Nakane
Department of Physics, Nagoya University, Nagoya 464-8602, Japan

Kazuki Nakazawa*
Department of Earth and Space Science, Osaka University, Osaka 560-0043, Japan

Hiroshi Kohno
Department of Physics, Nagoya University, Nagoya 464-8602, Japan
and Center for Spintronics Research Network (CSRN), Graduate School of Engineering Science, Osaka University, Osaka 560-8531, Japan

(Received 16 March 2020; revised manuscript received 4 May 2020; accepted 4 May 2020; published 21 May 2020)

Motivated by a recent experiment on manganese oxide thin films, we theoretically study the topological Hall effect in a weakly canted antiferromagnet with textured Néel ($\boldsymbol{n}$) and uniform ($\boldsymbol{l}$) components of magnetization. Treating the Néel texture by a spin gauge field and the uniform component perturbatively, we obtain an analytical expression for the topological Hall conductivity. The result is proportional to the emergent magnetic field, $\nabla \times \boldsymbol{A}_{\mathrm{AF}}$, where $A_{\mathrm{AF},i} = \boldsymbol{l} \cdot (\partial_i \boldsymbol{n} \times \boldsymbol{n})$ is an emergent vector potential in antiferromagnets, which consists of the spin-chirality density, $\hat{\boldsymbol{l}} \cdot (\partial_x \hat{\boldsymbol{l}} \times \partial_y \hat{\boldsymbol{l}})$, formed by the normalized uniform moment $\hat{\boldsymbol{l}} = \boldsymbol{l}/|\boldsymbol{l}|$, and one formed by the Néel and uniform components in the presence of spatial variation of canting. The result is discussed in comparison with the previous study on ferromagnets in the weak-coupling regime.

DOI: 10.1103/PhysRevB.101.174432

I. INTRODUCTION

The topological Hall effect (THE) [1,2] is a closely studied phenomena in conducting ferromagnets, realized when the conduction electrons interact with a ferromagnetic spin texture with nonzero spin chirality. This effect is used to electrically detect skyrmions [3,4], a particlelike spin texture with a quantized spin chirality, which is anticipated as an information carrier in next-generation magnetic memory devices.

Besides ferromagnets, antiferromagnets have recently gained high interests among researchers in the field of spintronics owing to their robustness to external perturbations, THz range spin dynamics, and the variety of hosting materials [5,6]. Despite its potentially rich physics, the THE in antiferromagnets is nonexistent due to the cancellation of the spin chiralities on different sublattices [7–9]. Recently, Vistoli *et al.* reported on the observation of THE in cerium-doped manganese oxide $Ca_{1-x}Ce_xMnO_3$, a *canted* antiferromagnet. They demonstrated that the skyrmionic magnetic bubbles formed by the ferromagnetic (canted) component are responsible for the observed Hall effect [10]. Theoretically, their experimental result cannot be explained by the strong-coupling (Berry-phase) formula due to Bruno *et al.* [2], but some of the features are well captured by the weak-coupling formula [11]. A theory on the THE in canted antiferromagnets is however absent.

In this paper, we theoretically investigate the Hall effect induced by spin chirality in canted antiferromagnets. Starting from a microscopic tight-binding Hamiltonian for electrons interacting with a textured canted antiferromagnetic (AF) background, we calculate the Hall conductivity using the Kubo formula. The spatial variation of the Néel vector $\boldsymbol{n}$, expressed by a spin gauge field, and the (locally) uniform moment $\boldsymbol{l}$ (magnetization) are treated perturbatively. The obtained topological Hall conductivity (THC) is linear in $\boldsymbol{l}$ and second order in electron scattering time. An emergent magnetic field responsible for the Hall motion is identified as $\boldsymbol{B}_{\mathrm{s}} = \nabla \times \boldsymbol{A}_{\mathrm{AF}}$, with an emergent vector potential, $A_{\mathrm{AF},i} = \boldsymbol{l} \cdot [(\partial_i \boldsymbol{n}) \times \boldsymbol{n}]$. The emergent field $\boldsymbol{B}_{\mathrm{s}}$ consists of spin-chirality density, $\hat{\boldsymbol{l}} \cdot (\partial_x \hat{\boldsymbol{l}} \times \partial_y \hat{\boldsymbol{l}})$, formed by the normalized uniform moment $\hat{\boldsymbol{l}} = \boldsymbol{l}/|\boldsymbol{l}|$, and a term $\sim (\nabla |\boldsymbol{l}| \times \boldsymbol{A}_{\mathrm{AF}})_z$ that arises from spatial variation of canting.

Because of the perturbative treatment of $\boldsymbol{l}$, the present theory is limited to the case of small ferromagnetic moment (due to canting). Quantitatively, the spin-splitting energy in the electron spectrum caused by the canting moment (i.e., $\boldsymbol{l}$) should be small compared to broadening due to impurity scattering [see Eq. (29)]. On the other hand, the magnitude of the AF moment can be arbitrary, and the result applies to both "strong-AF" and "weak-AF" regimes; in the former (latter) the AF gap is large (small) such that it significantly (negligibly) affects the electronic states at the Fermi level. An interesting result in relation to the above-mentioned experiment is that the topological Hall (TH) resistivity in the "strong-AF" regime is proportional to the square of the effective mass at low carrier density. Discussion will also be given in comparison with ferromagnets in the weak-coupling regime.

This paper is organized as follows. After explaining the model in Sec. II and outlining the calculation in Sec. III,

*Present address: Department of Applied Physics, The University of Tokyo, Tokyo 113-8656, Japan.

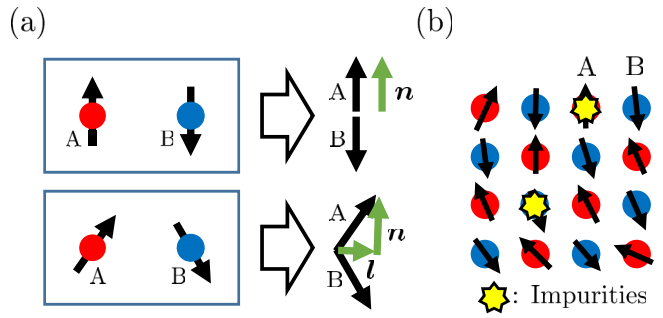

FIG. 1. Visual representations of the model. (a) Localized spins (black arrows) in a unit cell, which contains A- and B-sublattice sites (indicated by red and blue dots, respectively). A collinear antiferromagnet (upper panel) is described by the Néel vector $\boldsymbol{n}$ (staggered component), whereas a canted antiferromagnet (lower panel) requires the uniform component $\boldsymbol{l}$ (magnetization) as well. (b) Antiferromagnetic spin texture. Randomly distributed impurities, which act as on-site potentials, are also shown (yellow stars).

we present the result in Sec. IV, followed by discussion and summary in Secs. V and VI, respectively. Details of the calculation are described in the Supplemental Material [13].

II. MODEL

We consider electrons on a two-dimensional square lattice coupled to a static spin texture $\boldsymbol{S}_i$ in a canted antiferromagnet. The Hamiltonian is given by

$$\mathcal{H} = -t\sum_{\langle i,j\rangle}(c_i^\dagger c_j + \text{H.c.}) - J_{\text{sd}}\sum_i \boldsymbol{S}_i\cdot(c_i^\dagger\boldsymbol{\sigma}c_i) + \mathcal{H}_{\text{imp}}, \quad (1)$$

where $c_i^\dagger = (c_{i\uparrow}^\dagger, c_{i\downarrow}^\dagger)$ is the electron creation operator at site i. The first term describes the electron hopping (with amplitude t), and the sum $\sum_{\langle i,j\rangle}$ is taken over the pairs of nearest-neighbor sites, i and j. The second term describes the exchange coupling to localized spins $\boldsymbol{S}_i$ that form a static and slowly varying texture of the canted antiferromagnet. J_{sd} is the s-d exchange coupling constant and $\boldsymbol{\sigma} = (\sigma_x, \sigma_y, \sigma_z)$ are Pauli matrices.

We express $\boldsymbol{S}_i$ in terms of two "smooth" variables, $\boldsymbol{n}_i$ and $\boldsymbol{l}_i$,

$$\boldsymbol{S}_i = S[(-)^i\boldsymbol{n}_i + \boldsymbol{l}_i], \quad (-)^i = \begin{cases} 1, & i\in \text{A sublattice},\\ -1, & i\in \text{B sublattice}, \end{cases} \quad (2)$$

where S is the magnitude of the localized spin, $\boldsymbol{n}_i$ is the staggered moment (Néel vector), and $\boldsymbol{l}_i$ is the uniform moment (magnetization); see Fig. 1(a). We impose $|(-)^i\boldsymbol{n}_i + \boldsymbol{l}_i| = 1$, hence $\boldsymbol{n}_i^2 + \boldsymbol{l}_i^2 = 1$ and $\boldsymbol{n}_i\cdot\boldsymbol{l}_i = 0$. Throughout this study, we consider small canting $|\boldsymbol{l}_i| \ll 1$ and retain terms up to the linear order in $\boldsymbol{l}_i$ (neglecting $\boldsymbol{l}_i^2$), hence $|\boldsymbol{n}_i| = 1$ is assumed.

The last term in Eq. (1) is the coupling to randomly placed nonmagnetic impurities. We consider pointlike impurities described by

$$\mathcal{H}_{\text{imp}} = u_{\text{imp}}\sum_{i\in\text{C}} c_i^\dagger c_i, \quad (3)$$

where u_{imp} is the potential strength and C is the set of impurity positions [Fig. 1(b)]. The number of impurities on A and B sublattices is assumed to be equal. The impurity scattering introduces a finite scattering time τ, and also the spin dephasing time τ_φ for the electrons [see Eqs. (24) and (28) below].

To treat the spatial variation of the Néel vector $\boldsymbol{n}_i$, we move to a local spin frame by the $SU(2)$ rotation U_i that sorts the Néel vector to the z axis [12],

$$U_i^\dagger(\boldsymbol{n}_i\cdot\boldsymbol{\sigma})U_i = \sigma^z. \quad (4)$$

We also define the corresponding 3×3 matrix $\mathcal{R}_i$ that satisfies

$$U_i^\dagger\sigma^\alpha U_i = \mathcal{R}_i^{\alpha\beta}\sigma^\beta, \quad (5)$$

and an $SU(2)$ spin gauge field A_{ij} by

$$U_i^\dagger U_j = e^{iA_{ij}}. \quad (6)$$

This is associated with the hopping from site j to i, and satisfies $A_{ij} = -A_{ji}$. As stated, we assume slow spatial variation of $\boldsymbol{n}_i$ and $\boldsymbol{l}_i$, and thus A_{ij} is small, $|A_{ij}| \ll 1$. To first order in A_{ij}, the Hamiltonian reads

$$\mathcal{H} = \mathcal{H}_0 + \mathcal{H}_A + \mathcal{H}_{\boldsymbol{l}} + \mathcal{H}_{\text{imp}}, \quad (7)$$

with

$$\mathcal{H}_0 = -t\sum_{\langle i,j\rangle}(\tilde{c}_i^\dagger\tilde{c}_j + \text{H.c.}) - J\sum_i(-)^i\tilde{c}_i^\dagger\sigma^z\tilde{c}_i, \quad (8)$$

$$\mathcal{H}_A = -it\sum_{\langle i,j\rangle}(\tilde{c}_i^\dagger A_{ij}\tilde{c}_j + \tilde{c}_j^\dagger A_{ji}\tilde{c}_i), \quad (9)$$

$$\mathcal{H}_{\boldsymbol{l}} = -J\sum_i(\mathcal{R}_i^{-1}\boldsymbol{l}_i)\cdot(\tilde{c}_i^\dagger\boldsymbol{\sigma}\tilde{c}_i), \quad (10)$$

where $J = J_{\text{sd}}S$. We introduced the electron operator $\tilde{c}_i = U_i^\dagger c_i$ in the rotated frame. We further assume that the canting is small, $|\boldsymbol{l}| \ll 1$, and treat $\mathcal{H}_A$ and $\mathcal{H}_{\boldsymbol{l}}$ perturbatively. Introducing the sublattice representation,

$$\tilde{c}_i = \begin{cases} a_i, & i\in\text{A sublattice},\\ b_i, & i\in\text{B sublattice}, \end{cases} \quad (11)$$

and writing $\psi_{\boldsymbol{k}} = {}^t(a_{\boldsymbol{k}\uparrow} \;\; a_{\boldsymbol{k}\downarrow} \;\; b_{\boldsymbol{k}\uparrow} \;\; b_{\boldsymbol{k}\downarrow})$ with the Fourier components $a_{\boldsymbol{k}\sigma}$ and $b_{\boldsymbol{k}\sigma}$ (see below for explicit definition), the Hamiltonian is written as

$$\mathcal{H}_0 = \sum_{\boldsymbol{k}}\psi_{\boldsymbol{k}}^\dagger(\varepsilon_{\boldsymbol{k}}\tau_1 - J\tau_3\sigma^3)\psi_{\boldsymbol{k}}, \quad (12)$$

$$\mathcal{H}_A = \sum_{i=x,y}\sum_{\boldsymbol{k},\boldsymbol{q}}(\partial_i\varepsilon_{\boldsymbol{k}})(\psi_{\boldsymbol{k}_+}^\dagger\tau_1\psi_{\boldsymbol{k}_-})A_i(\boldsymbol{q}), \quad (13)$$

$$\mathcal{H}_{\boldsymbol{l}} = -J\sum_{\boldsymbol{k},\boldsymbol{q}}(\mathcal{R}^{-1}\boldsymbol{l})_{\boldsymbol{q}}\cdot(\psi_{\boldsymbol{k}_+}^\dagger\boldsymbol{\sigma}\psi_{\boldsymbol{k}_-}), \quad (14)$$

$$\mathcal{H}_{\text{imp}} = u_{\text{imp}}\sum_{\boldsymbol{k},\boldsymbol{k}'}\psi_{\boldsymbol{k}}^\dagger\left[\sum_{r=\text{A,B}}P_r\rho_r^{\text{imp}}(\boldsymbol{k}'-\boldsymbol{k})\right]\psi_{\boldsymbol{k}'}, \quad (15)$$

where $\varepsilon_{\boldsymbol{k}} = -2t(\cos k_x + \cos k_y)$, $\boldsymbol{k}_\pm = \boldsymbol{k}\pm\frac{\boldsymbol{q}}{2}$, and τ_i and σ^α are Pauli matrices that act in sublattice (A or B) and spin ($\uparrow$ or $\downarrow$) spaces, respectively. We set the lattice constant to unity. In $\mathcal{H}_{\text{imp}}$, $P_{\text{A,B}} = (\tau_0\pm\tau_3)/2$ is the

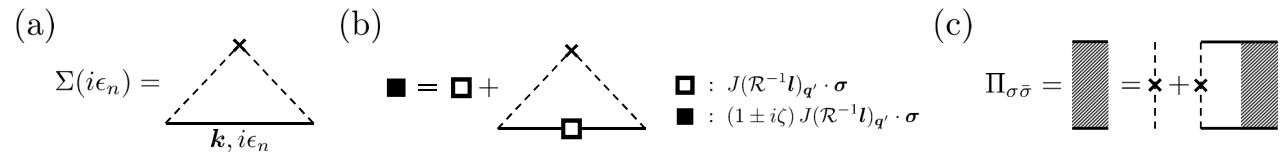

FIG. 2. Feynman diagrams for the treatment of random impurities. The solid line is the electron Green's function, and the dashed line with a cross represents impurity scattering. (a) Self-energy in the Born approximation. (b) Coupling to the uniform moment, Eq. (14), and impurity correction. The empty (filled) square represents the bare (dressed) vertex. The second term is regarded as a self-energy which is first order in $\boldsymbol{l}$. (c) The ladder-type vertex correction. The upper (lower) solid line is the retarded (advanced) Green's function with spin σ ($\bar{\sigma}$).

projection operator to each sublattice, and $\rho^{\rm imp}_{\rm A,B}(\boldsymbol{k}'-\boldsymbol{k}) = \frac{2}{N}\sum_{j\in({\rm A\ or\ B})\cap{\rm C}} e^{i(\boldsymbol{k}'-\boldsymbol{k})\cdot\boldsymbol{r}_j}$ is the Fourier component of the impurity distribution. We define the Fourier transform of the electron operators by

$$a_i = \sqrt{\frac{2}{N}}\sum_{\boldsymbol{k}} a_{\boldsymbol{k}} e^{i\boldsymbol{k}\cdot\boldsymbol{r}_i}, \quad a_{\boldsymbol{k}} = \sqrt{\frac{2}{N}}\sum_{i\in A} a_i e^{-i\boldsymbol{k}\cdot\boldsymbol{r}_i}, \tag{16}$$

$$b_i = \sqrt{\frac{2}{N}}\sum_{\boldsymbol{k}} b_{\boldsymbol{k}} e^{i\boldsymbol{k}\cdot\boldsymbol{r}_i}, \quad b_{\boldsymbol{k}} = \sqrt{\frac{2}{N}}\sum_{i\in B} b_i e^{-i\boldsymbol{k}\cdot\boldsymbol{r}_i}, \tag{17}$$

where the $\boldsymbol{k}$-integral is taken in the reduced Brillouin zone, $|k_x + k_y| \leqslant \pi$, and N is the total number of sites. With this definition, either $a_{\boldsymbol{k}}$ or $b_{\boldsymbol{k}}$ lacks periodicity (e.g., $b_{\boldsymbol{k}+\boldsymbol{Q}_{\rm AF}} = -b_{\boldsymbol{k}}$) with respect to the AF wave vector $\boldsymbol{Q}_{\rm AF} = (\pi, \pi)$, but, in physical quantities, such unsatisfactory operator is always associated with a compensating factor (such as e^{ik_x}) that recovers the periodicity as a whole. Similarly, we define the Fourier transform of the gauge field and uniform moment by

$$A_{ij} = \sum_{\boldsymbol{q}} A_\mu(\boldsymbol{q})\, e^{i\boldsymbol{q}\cdot(\boldsymbol{r}_i+\boldsymbol{r}_j)/2}, \tag{18}$$

$$\left(\mathcal{R}_i^{-1}\boldsymbol{l}_i\right) = \sum_{\boldsymbol{q}} (\mathcal{R}^{-1}\boldsymbol{l})_{\boldsymbol{q}}\, e^{i\boldsymbol{q}\cdot\boldsymbol{r}_i}, \tag{19}$$

where $\hat{\mu} = \boldsymbol{r}_j - \boldsymbol{r}_i$, and A_{ij} is supposed to live on the link centered at $(\boldsymbol{r}_i + \boldsymbol{r}_j)/2$. We expand A_μ in terms of Pauli matrices,

$$A_\mu(\boldsymbol{q}) = \sum_{\alpha=x,y,z} A^\alpha_\mu(\boldsymbol{q})\,\frac{\sigma^\alpha}{2} \equiv \boldsymbol{A}_\mu \cdot \frac{\boldsymbol{\sigma}}{2}. \tag{20}$$

Usually, A^z_μ is called the adiabatic component and $\boldsymbol{A}^\perp_\mu \equiv (A^x_\mu, A^y_\mu, 0)$ the nonadiabatic component. In the following calculation, the nonadiabatic components inevitably enter the expression of THC since a spin flip induced by $\mathcal{R}^{-1}\boldsymbol{l}$ needs to be undone by $\boldsymbol{A}^\perp_\mu$ in Feynman diagrams (see below).

III. CALCULATION

To calculate the THC, we use Kubo formula for electrical conductivity,

$$\sigma_{\mu\nu}(\boldsymbol{Q},\omega) = \frac{K^R_{\mu\nu}(\boldsymbol{Q},\omega) - K^R_{\mu\nu}(\boldsymbol{Q},0)}{i\omega},$$
$$K^R_{\mu\nu}(\boldsymbol{Q},\omega) = i\int_0^\infty dt\, e^{i(\omega+i0)t}\langle[\tilde{j}_\mu(\boldsymbol{Q},t),\ \tilde{j}_\nu(\boldsymbol{0},0)]\rangle, \tag{21}$$

and extract the antisymmetric part, $\frac{1}{2}(\sigma_{xy} - \sigma_{yx})$, which will also be denoted by σ_{xy}. The Hall conductivity given above looks at the Fourier $\boldsymbol{Q}$ component of the electric current in the μ direction,

$$\tilde{j}_\mu(\boldsymbol{Q}) = -e\sum_{\boldsymbol{k}} \psi^\dagger_{\boldsymbol{k}-\frac{\boldsymbol{Q}}{2}}[(\partial_\mu\varepsilon_{\boldsymbol{k}})\tau_1]\psi_{\boldsymbol{k}+\frac{\boldsymbol{Q}}{2}}$$
$$- e\sum_{\boldsymbol{k},\boldsymbol{q}} \psi^\dagger_{\boldsymbol{k}-\frac{\boldsymbol{Q}}{2}+\frac{\boldsymbol{q}}{2}}\left[\left(\partial^2_\mu\varepsilon_{\boldsymbol{k}}\right)A_\mu(\boldsymbol{q})\tau_1\right]\psi_{\boldsymbol{k}+\frac{\boldsymbol{Q}}{2}-\frac{\boldsymbol{q}}{2}}, \tag{22}$$

in response to a uniform electric field in the ν direction. The wave vector $\boldsymbol{Q}$ of the current is fed by the spin texture, $\boldsymbol{n}_i$ or $\boldsymbol{l}_i$ (more precisely, $\boldsymbol{A}_\mu$ or $\mathcal{R}^{-1}\boldsymbol{l}_i$), and ω is the frequency of the applied electric field. To obtain the d.c. THC, we take the limit $\boldsymbol{Q} \to 0$, followed by $\omega \to 0$.

For the calculation, we employ the Green's functions of $\mathcal{H}_0 + \mathcal{H}_{\rm imp}$, in which the effects of the impurities ($\mathcal{H}_{\rm imp}$) are considered by the Born approximation in the self-energy [see Fig. 2(a)]. The retarded Green's function in the rotated frame is given by

$$G^R_{\boldsymbol{k}} = \mu^R + T^R_{\boldsymbol{k}}\tau_1 + J^R\tau_3\sigma^3, \tag{23}$$

where $\mu^R = (\mu + i\gamma_0)/D^R_{\boldsymbol{k}}$, $T^R_{\boldsymbol{k}} = \varepsilon_{\boldsymbol{k}}/D^R_{\boldsymbol{k}}$, $J^R = (-J + i\gamma_3)/D^R_{\boldsymbol{k}}$ with $D^R_{\boldsymbol{k}} = (\mu + i\gamma_0)^2 - \varepsilon^2_{\boldsymbol{k}} - (J - i\gamma_3)^2$. The damping constants are given by $\gamma_0 = \frac{\pi}{2}n_{\rm imp}u^2_{\rm imp}\nu$ and $\gamma_3 = \frac{J}{\mu}\gamma_0$, where $\nu = \nu(\mu) = \frac{2}{N}\sum_{\boldsymbol{k}}\delta(|\mu| - E_{\boldsymbol{k}})$ is the density of states and $n_{\rm imp}$ is the impurity concentration.

We assume that the effects of impurity scattering are weak, and approximate as $D^R_{\boldsymbol{k}} \simeq \mu^2 - E^2_{\boldsymbol{k}} + 2i\mu\gamma$, where

$$\gamma = \gamma_0 + \frac{J}{\mu}\gamma_3 = \frac{\mu^2 + J^2}{\mu^2}\gamma_0 \equiv \frac{1}{2\tau} \tag{24}$$

is the damping of electrons in the AF band, and

$$\pm E_{\boldsymbol{k}} = \pm\sqrt{\varepsilon^2_{\boldsymbol{k}} + J^2} \tag{25}$$

is the energy of the upper and lower electron bands ("AF bands") in a uniform AF state without canting; the two bands are separated by a gap $2J$ ("AF gap"), and both bands are spin degenerate. The chemical potential μ is measured from the AF gap center.

There is one more correction that may be classified as self-energy. It is expressed by Fig. 2(b) and contains an $\boldsymbol{l}$ vertex. Together with the bare $\boldsymbol{l}$ vertex, $(\mathcal{R}^{-1}\boldsymbol{l})\cdot\boldsymbol{\sigma}$, it gives $(1 \pm i\zeta)J(\mathcal{R}^{-1}\boldsymbol{l})\cdot\boldsymbol{\sigma}$, where $\zeta \sim O(\gamma)$ comes from the impurity correction (see the Supplemental Material [13] for the expression of ζ). The sign $+$ $(-)$ corresponds to the retarded (advanced) Green's function. Although this correction can in principle contribute to the leading terms, it did not play an essential role in the result.

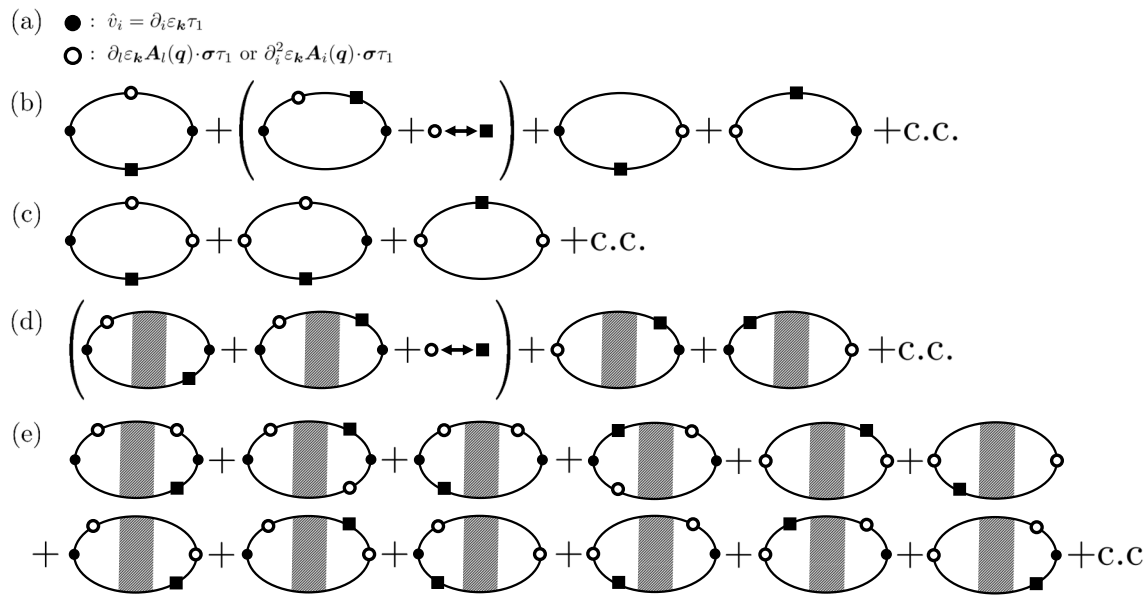

FIG. 3. Feynman diagrams for the topological Hall conductivity in weakly canted antiferromagnets. (a) Definition of vertices. The filled circle represents the current vertex, $(\partial_i \varepsilon_{\boldsymbol{k}})\tau_1$. The empty circle represents the vertex that contains the spin gauge field $\boldsymbol{A}$ coming from either the perturbation Hamiltonian $(\partial_l \varepsilon_{\boldsymbol{k}})\boldsymbol{A}_l(\boldsymbol{q}) \cdot \boldsymbol{\sigma}\tau_1$ or the current vertex $(\partial_i^2 \varepsilon_{\boldsymbol{k}})\boldsymbol{A}_i(\boldsymbol{q}) \cdot \boldsymbol{\sigma}\tau_1$. In each diagram in (b–e), the solid line in the upper (lower) half represents the retarded (advanced) Green's function, and the left and right vertices come from the current operators in the Kubo formula. Arrows usually attached to the electron lines are suppressed for simplicity. (b) Diagrams of first order in $\boldsymbol{A}$ and first order in $\boldsymbol{l}$. (c) Diagrams of second order in $\boldsymbol{A}$ and first order in $\boldsymbol{l}$. (d) Diagrams of first order in $\boldsymbol{A}$ and first order in $\boldsymbol{l}$ with ladder VC. (e) Diagrams of second order in $\boldsymbol{A}$ and first order in $\boldsymbol{l}$ with ladder VC. These diagrams contain gauge-invariant and gauge-noninvariant terms. There occur cancellations of gauge-noninvariant terms between (b) and (c), and between (d) and (e).

For consistency with the Born approximation [Fig. 2(a)], one needs to consider vertex corrections (VC) due to impurity scattering. As shown in Fig. 2(c), we take a ladder sum since each term contributes by the same order of magnitude [Fig. 2(c)]. The relevant processes have two Green's functions with opposite spin and opposite causality (retarded or advanced), and the result is given by [13]

$$\Pi_{\sigma\bar{\sigma}}(\boldsymbol{q}, \omega) = \frac{4 n_{\rm imp} u_{\rm imp}^2}{\left(Dq^2 - i\omega + \tau_\varphi^{-1}\right)\tau} \frac{\mu^2 + J^2}{\mu^2 - J^2} \tag{26}$$

$$\simeq 4 n_{\rm imp} u_{\rm imp}^2 \frac{\mu^2 + J^2}{\mu^2 - J^2} \frac{\tau_\varphi}{\tau}, \tag{27}$$

where

$$\tau_\varphi = \frac{\mu^2 - J^2}{2J^2}\tau = \frac{\mu}{4J\gamma_3} \frac{\mu^2 - J^2}{\mu^2 + J^2}, \tag{28}$$

is the spin dephasing time [14] and D is the diffusion constant. Note that the spin dephasing arises from scattering from normal (spin-independent) impurities. In Eq. (26), q actually represents $|\boldsymbol{q}|$, $|\boldsymbol{q}'|$ or $|\boldsymbol{q} \pm \boldsymbol{q}'|$, where $\boldsymbol{q}$ and $\boldsymbol{q}'$ are wave vectors fed by $\boldsymbol{A}_l(\boldsymbol{q})$ and $(\mathcal{R}^{-1}\boldsymbol{l})_{\boldsymbol{q}'}$, respectively, which are assumed very small [see Eq. (30) below] and will finally be neglected. We also let $\omega \to 0$ to obtain the d.c. THC. Note that the result, Eq. (27), is proportional to τ_φ.

Before proceeding, let us make explicit the range of validity of the present calculation. First, the perturbative treatment of $\boldsymbol{l}$ is justified when

$$J|\boldsymbol{l}| < \gamma, \tag{29}$$

meaning that the spin-splitting energy, $J|\boldsymbol{l}|$, caused by the canting should be smaller than the broadening γ. This corresponds to the weak-coupling condition as to the ferromagnetic moment [11]. Second, the spatial variation of the spin texture should be slow and must satisfy

$$q\ell_\varphi < 1, \tag{30}$$

where q is the typical magnitude of the wave number of the texture ($\boldsymbol{n}$ and $\boldsymbol{l}$), and $\ell_\varphi = \sqrt{D\tau_\varphi}$ is the spin dephasing length. This justifies the approximation made in going from Eq. (26) to Eq. (27). This is the condition for the locality of the emergent field [11].

Now, with the Green's functions and the VC in hand, one can calculate the THC. The diagrams are shown in Fig. 3, which are classified into two types; the ones without VC [Figs. 3(b) and 3(c)], whose contribution is denoted by $\sigma_{xy}^{(0)}$, and those with VC [Figs. 3(d) and 3(e)], denoted by $\sigma_{xy}^{(\rm VC)}$. We are interested in the leading-order contribution in the spatial gradient of the texture (which comes from the spin gauge field A_μ^α or the wave vector q), the electron damping γ, and the uniform moment $|\boldsymbol{l}|$. See the Supplemental Material [13] for the details of calculation.

IV. RESULT

The result is given by

$$\sigma_{xy} = \sigma_{xy}^{(0)} + \sigma_{xy}^{(\rm VC)}, \tag{31}$$

$$\sigma_{xy}^{(0)} = e^2 \langle B_{{\rm s},z} \rangle J |\mu| \, \tau^2 \, \eta, \tag{32}$$

$$\sigma_{xy}^{(\rm VC)} = \tfrac{1}{2} e^2 \langle B_{{\rm s},z} \rangle J |\mu| \, \tau \tau_\varphi \, \eta', \tag{33}$$

which consists of $\sigma_{xy}^{(0)}$ (without VC) and $\sigma_{xy}^{(\mathrm{VC})}$ (with VC). Both are first order in the uniform moment $|\boldsymbol{l}|$ and second order in the relaxation time τ. The information of the texture is contained in the emergent magnetic field,

$$B_{\mathrm{s},z} = (\nabla \times \boldsymbol{A}_{\mathrm{AF}})_z \tag{34}$$

$$= \partial_x \boldsymbol{l} \cdot (\partial_y \boldsymbol{n} \times \boldsymbol{n}) - \partial_y \boldsymbol{l} \cdot (\partial_x \boldsymbol{n} \times \boldsymbol{n}), \tag{35}$$

via the spatial average $\langle B_{\mathrm{s},z} \rangle$. Here,

$$\boldsymbol{A}_{\mathrm{AF}} = \begin{pmatrix} \boldsymbol{l} \cdot (\partial_x \boldsymbol{n} \times \boldsymbol{n}) \\ \boldsymbol{l} \cdot (\partial_y \boldsymbol{n} \times \boldsymbol{n}) \\ \boldsymbol{l} \cdot (\partial_z \boldsymbol{n} \times \boldsymbol{n}) \end{pmatrix} \tag{36}$$

may be regarded as an emergent vector potential in antiferromagnets [15]. The i component $A_{\mathrm{AF},i} = \partial_i \boldsymbol{n} \cdot (\boldsymbol{n} \times \boldsymbol{l})$ arises if, as one moves in the i direction, $\boldsymbol{n}$ develops a component perpendicular to both $\boldsymbol{n}$ and $\boldsymbol{l}$, namely, if $\boldsymbol{n}$ rotates around $\boldsymbol{l}$.

As shown in Appendix, the emergent field $B_{\mathrm{s},z}$ enjoys a more interesting expression,

$$B_{\mathrm{s},z} = |\boldsymbol{l}|\, \hat{\boldsymbol{l}} \cdot (\partial_x \hat{\boldsymbol{l}} \times \partial_y \hat{\boldsymbol{l}}) + [(\nabla |\boldsymbol{l}|) \times (\boldsymbol{A}_{\mathrm{AF}}/|\boldsymbol{l}|)]_z. \tag{37}$$

The first term is proportional to the spin chirality density, $\hat{\boldsymbol{l}} \cdot (\partial_x \hat{\boldsymbol{l}} \times \partial_y \hat{\boldsymbol{l}})$, formed by the (normalized) uniform component $\hat{\boldsymbol{l}} \equiv \boldsymbol{l}/|\boldsymbol{l}|$. Note that it is *linearly* proportional to $|\boldsymbol{l}|$ (the magnitude of $\boldsymbol{l}$). The second term arises from spatial variation of the degree of canting (i.e., $|\boldsymbol{l}|$). Its combination with $\boldsymbol{A}_{\mathrm{AF}}$ can also give rise to scalar spin chirality. Examples of spin texture that contributes to these terms will be given in Sec. V B. We here note that the form of Eq. (36) is in harmony with the kinetic term in the Lagrangian of antiferromagnets, which is given to leading order of $\boldsymbol{l}$ by $-2\hbar S\, \boldsymbol{l} \cdot (\dot{\boldsymbol{n}} \times \boldsymbol{n})$ [16–18]. The time-component counterpart of Eq. (36) has also been found to appear in the electromotive force generated by AF spin dynamics [19].

The coefficients, η and η', in Eqs. (32) and (33) are obtained as

$$\eta = C \frac{t^2 \nu}{|\mu|} \langle\!\langle 1 - \cos k_x \cos k_y \rangle\!\rangle_{\mathrm{FS}}$$

$$= \frac{C}{(2\pi)^2 \tilde{\mu}} \left[2K\left(\frac{1-\tilde{\mu}}{1+\tilde{\mu}}\right) - (1+\tilde{\mu}) E\left(\frac{1-\tilde{\mu}}{1+\tilde{\mu}}\right) \right], \tag{38}$$

$$\eta' = C \frac{t^2 \nu}{|\mu|} \langle\!\langle 1 - \cos^2 k_x \rangle\!\rangle_{\mathrm{FS}}$$

$$= -\frac{C}{(2\pi)^2 \tilde{\mu}} \left[2\tilde{\mu} K\left(\frac{1-\tilde{\mu}}{1+\tilde{\mu}}\right) - (1+\tilde{\mu}) E\left(\frac{1-\tilde{\mu}}{1+\tilde{\mu}}\right) \right], \tag{39}$$

where $\langle\!\langle \cdots \rangle\!\rangle_{\mathrm{FS}} \equiv \sum_{\boldsymbol{k}} (\cdots) \delta(|\mu| - E_{\boldsymbol{k}}) / \sum_{\boldsymbol{k}} \delta(|\mu| - E_{\boldsymbol{k}})$ is the Fermi-surface average, C is a constant given by

$$C = \frac{4J^2(\mu^2 - J^2)}{\mu^2(\mu^2 + J^2)}, \tag{40}$$

and $K(k) = \int_0^1 \frac{dt}{\sqrt{(1-t^2)(1-k^2t^2)}}$ and $E(k) = \int_0^1 \frac{\sqrt{1-k^2t^2}}{\sqrt{1-t^2}} dt$ are the complete elliptic integrals. We defined a reduced chemical potential $\tilde{\mu} = \sqrt{\mu^2 - J^2}/4t$, which takes $\tilde{\mu} = 1$ at the band bottom/top ($\mu = \pm\sqrt{(4t)^2 + J^2}$), and $\tilde{\mu} = 0$ at the AF gap edge ($\mu = \pm J$).

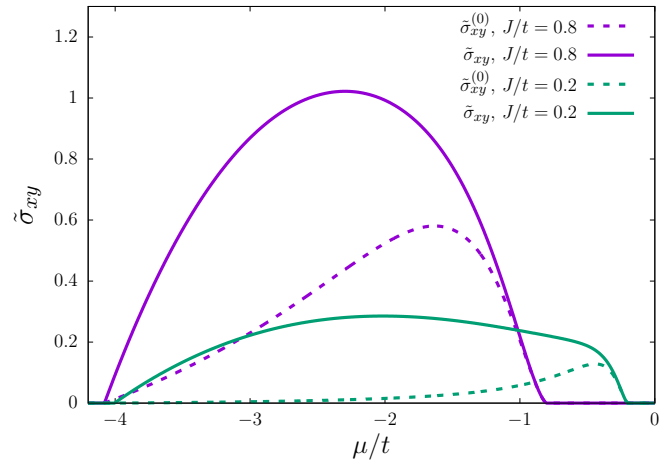

FIG. 4. Normalized topological Hall conductivity, $\tilde{\sigma}_{xy} = \sigma_{xy}\tilde{\gamma}^2/(e^2\langle B_{\mathrm{s},z}\rangle)$, where $\tilde{\gamma} \equiv \pi n_{\mathrm{imp}} u_{\mathrm{imp}}^2/(2t^2)$, plotted as a function of chemical potential μ for $J/t = 0.2$ and 0.8. The dashed (solid) lines represent $\tilde{\sigma}_{xy}^{(0)}$ ($\tilde{\sigma}_{xy} = \tilde{\sigma}_{xy}^{(0)} + \tilde{\sigma}_{xy}^{(\mathrm{VC})}$) without VC (including VC). They are even functions of μ (symmetric about the AF gap center, $\mu = 0$), hence plotted only for the lower AF band ($\mu < 0$). When J/t is small (e.g., $J/t = 0.2$ in this figure), $\sigma_{xy}^{(\mathrm{VC})}$ dominates $\sigma_{xy}^{(0)}$ in a wide range of μ, whereas when $J/t \sim 1$ (e.g., $J/t = 0.8$ in this figure), the two are comparable in magnitude.

In Fig. 4, $\sigma_{xy}^{(0)}$ (without VC) and $\sigma_{xy} = \sigma_{xy}^{(0)} + \sigma_{xy}^{(\mathrm{VC})}$ (including VC) are plotted as functions of μ. Each curve is normalized as $\tilde{\sigma}_{xy} = \sigma_{xy}\tilde{\gamma}^2/(e^2\langle B_{\mathrm{s},z}\rangle)$, where $\tilde{\gamma} \equiv \pi n_{\mathrm{imp}} u_{\mathrm{imp}}^2/(2t^2) = \gamma_0/(t^2\nu)$ is a dimensionless damping parameter. Overall, each curve shows a broad peak. When J is comparable to t, $\sigma_{xy}^{(0)}$ and $\sigma_{xy}^{(\mathrm{VC})}$ are comparable but the peak position is relatively shifted. In a closer look, whether the VC is important or not depends on the chemical potential μ. The dashed curves for $\sigma_{xy}^{(0)}$ are peaked at around $\mu = -2J$, which separates the two characteristic regions. When μ is close to the AF gap, $-2J < \mu < -J$, the effects of VC are negligible, but they become quantitatively very important for $\mu < -2J$. We also see that the VC is more important for smaller J. To sum up, we may say that the VC is important (negligible) for electrons with good (poor) itineracy.

The above discussion may be put in a more "theoretical" form. Since $\sigma_{xy}^{(\mathrm{VC})}/\sigma_{xy}^{(0)} \simeq \tau_\varphi/\tau$ (η and η' are comparable in size), the ratio τ_φ/τ determines the relative importance of the two contributions and leads to the classification,

$$\text{Weak-AF regime}: \quad \tau_\varphi \gtrsim \tau \quad \text{or} \quad |\mu| \gtrsim \sqrt{3}J,$$

$$\text{Strong-AF regime}: \quad \tau_\varphi \lesssim \tau \quad \text{or} \quad |\mu| \lesssim \sqrt{3}J.$$

From a closer look at Fig. 4 (in particular, the curves for $J/t = 0.8$), one may see that $|\mu| = \sqrt{3}J$ gives a more precise boundary.

In Fig. 5, we show the normalized THC $\tilde{\sigma}_{xy}$ (including VC) and the normalized Hall angle $\tilde{\alpha}_{xy} = \tilde{\sigma}_{xy}/\tilde{\sigma}_{xx}$ in the plane of band filling n and J/t. (The diagonal conductivity is given by $\sigma_{xx} = 2e^2 D\nu$ [13], which is normalized as $\tilde{\sigma}_{xx} = \sigma_{xx}\tilde{\gamma}/e^2$.) As seen, the Hall conductivity $\tilde{\sigma}_{xy}$ is peaked at around $J/t = 1 \sim 2$ and $n = 0.2 \sim 0.3$. The Hall angle α_{xy} shows a plateau for $J/t \gtrsim 2$ and $n \lesssim 0.4$, and approaches a finite value as $n \to 0$. The TH resistivity is thus inversely proportional to n (for fixed

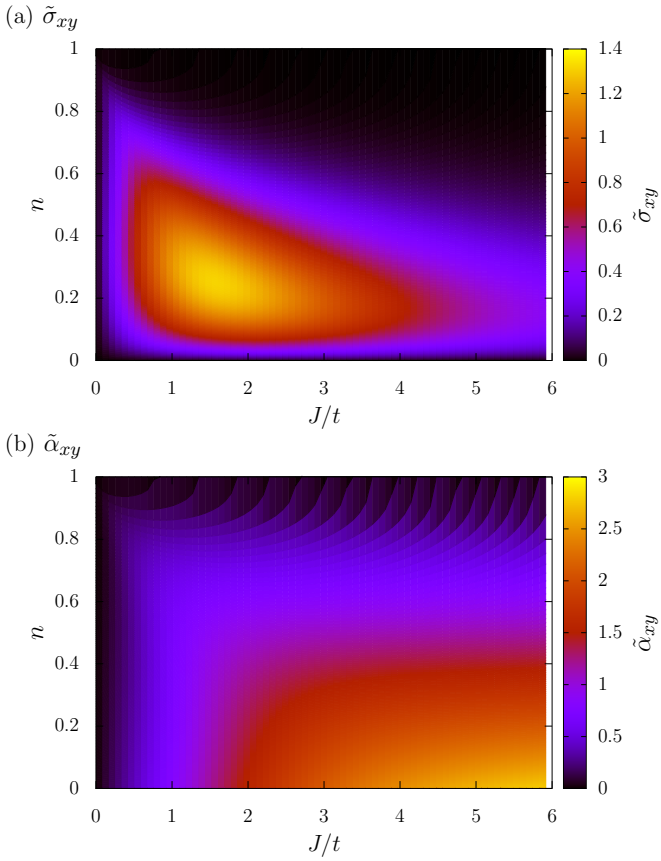

FIG. 5. Color plots in the plane of band filling n and J/t. ($n = 1$ corresponds to completely filled lower and empty upper AF bands.) (a) Normalized topological Hall conductivity, $\tilde{\sigma}_{xy} = \tilde{\sigma}_{xy}^{(0)} + \tilde{\sigma}_{xy}^{(\mathrm{VC})}$. (b) Normalized Hall angle, $\tilde{\alpha}_{xy} = \tilde{\sigma}_{xy}/\tilde{\sigma}_{xx}$, where $\tilde{\sigma}_{xx} = \sigma_{xx}\tilde{\gamma}/e^2$. The Hall angle is given by $\alpha_{xy} = \tilde{\alpha}_{xy}\langle B_{\mathrm{s},z}\rangle/\tilde{\gamma}$.

τ and the effective mass) near the band bottom ($n \ll 1$). It also shows a divergent behavior as $n \to 1$.

V. DISCUSSION

In this section, we discuss the present results for canted antiferromagnets in relation to the previous work on ferromagnets in the weak-coupling regime [11]. We also present an example of spin texture that gives rise to each term of the emergent field in Eq. (37).

A. Comparison with weak-coupling ferromagnets

First, the characteristic features of THC in weak-coupling ferromagnets [11] are summarized as follows.

(i) Like in Bruno's strong-coupling result, the emergent magnetic field is given by the spin chirality even at weak coupling.

(ii) The THC is linearly proportional to the uniform moment (or M, the exchange splitting). This is a nonperturbative effect governed by the precession-dominated propagation of transverse spin density of electrons (see below for details).

(iii) The THC is proportional to the inverse effective (band) mass, $\sigma_{xy} \propto (m^*)^{-1}$, and the TH resistivity is proportional to the effective mass, $\rho_{xy} \propto m^*$ (for fixed carrier density and scattering time).

In the following, we discuss the present results for canted antiferromagnets.

1. Emergent field in weakly canted antiferromagnet

The THE is absent in locally collinear (uncanted) antiferromagnets because of the cancellation between opposite chirality components on the two sublattices [7–9]. If the AF moments are canted, then this cancellation becomes imperfect and the THC arises, as we have seen, at linear order in $|\boldsymbol{l}|$. One might think that it should start from third order in $|\boldsymbol{l}|$ considering the results of weak-coupling (perturbative) treatment [20–22]. This is where we see the AF moment in play, namely, the Néel vector and the uniform moment cooperate to give rise to a nonvanishing spin chirality in the antiferromagnet.

The terms linear in $|\boldsymbol{l}|$ can be obtained by the perturbative treatment of $\boldsymbol{l}$, as adopted in this paper. This is valid in the "weak-coupling" (weakly canted) regime, $J|\boldsymbol{l}|\tau \ll 1$. (This corresponds to $M\tau < 1$ for ferromagnets.)

The form of the emergent magnetic field can be obtained based on symmetry. We focus on terms which are first order in $\boldsymbol{l}$ and second order in spatial gradient of $\boldsymbol{n}$ or $\boldsymbol{l}$, and consider in the rotated frame a perturbative expansion in terms of the $SU(2)$ gauge field (A_i^α), the magnetization $\tilde{\boldsymbol{l}} \equiv \mathcal{R}^{-1}\boldsymbol{l}$, and spatial gradient ∂_j. First, the (global) spin-rotation symmetry around z axis allows three terms, giving

$$\begin{aligned}\sigma_{ij} &= c_1(\partial_i \boldsymbol{A}_j - \partial_j \boldsymbol{A}_i)\cdot\tilde{\boldsymbol{l}} + c_2(\boldsymbol{A}_j\cdot\partial_i\tilde{\boldsymbol{l}} - \boldsymbol{A}_i\cdot\partial_j\tilde{\boldsymbol{l}}) \\ &\quad + c_3(\boldsymbol{A}_i\times\boldsymbol{A}_j)\cdot\tilde{\boldsymbol{l}} \\ &= (c_1+c_3)(\partial_i\boldsymbol{A}_j^\perp - \partial_j\boldsymbol{A}_i^\perp)\cdot\tilde{\boldsymbol{l}} \\ &\quad + c_2(\boldsymbol{A}_j^\perp\cdot\partial_i\tilde{\boldsymbol{l}} - \boldsymbol{A}_i^\perp\cdot\partial_j\tilde{\boldsymbol{l}}),\end{aligned} \tag{41}$$

where c_n's are coefficients. Since the $SU(2)$ field strength vanishes, $\boldsymbol{F}_{ij} \equiv \partial_i\boldsymbol{A}_j - \partial_j\boldsymbol{A}_i - \boldsymbol{A}_i\times\boldsymbol{A}_j = 0$ [11,23], the first term and the third term are the same, hence combined in the last expression. The $U(1)$ gauge invariance (invariance under local spin rotaion around the z axis [23]) requires $c_1 + c_3 = c_2$, and only in this case, one obtains a gauge-invariant form,

$$\sigma_{ij} = c_2\{\partial_i(\boldsymbol{A}_j^\perp\cdot\tilde{\boldsymbol{l}}) - \partial_j(\boldsymbol{A}_i^\perp\cdot\tilde{\boldsymbol{l}})\}. \tag{42}$$

As shown in the Supplemental Material [13], this is actually the case. Note that c_2 ($= c_1 + c_3$), though evaluated at $\tilde{\boldsymbol{l}} = \boldsymbol{0}$, does not vanish in general (in contrast to the case of ferromagnets [11]) since $\boldsymbol{n}$ is well-developed and breaks the symmetry between the z direction and the x, y directions in the rotated spin space. Therefore, unlike in Ref. [11], the $\boldsymbol{l}$-linear contribution survives at the perturbative level. From Eq. (42), we can read off the emergent vector potential,

$$A_{\mathrm{AF},i} = \boldsymbol{A}_i^\perp\cdot\tilde{\boldsymbol{l}} = \boldsymbol{l}\cdot(\partial_i\boldsymbol{n}\times\boldsymbol{n}), \tag{43}$$

where we used the identity, $\mathcal{R}\boldsymbol{A}_i^\perp = \partial_i\boldsymbol{n}\times\boldsymbol{n}$ [24]. This is nothing but Eq. (36).

When $J \ll |\mu|$, which we call "weak-AF" regime, the Néel component is negligible and the full spin-rotation symmetry is recovered. Thus, c_2 ($= c_1 + c_3$) vanishes like $\sim J^3$ as $J \to 0$ (for $\sigma_{xy}^{(0)}$, see the next subsection), and the $\boldsymbol{l}$-linear terms disappear. This corresponds to what has been observed in ferromagnets in the weak-coupling regime (at the perturbative level without spin diffusion propagator).

2. Propagation of transverse spin density

As seen, $\boldsymbol{l}$ is required for the THE, which flips electron spin with respect to the Néel vector direction. This means that the THE involves a process of transverse spin propagation (perpendicular to the Néel vector). Such processes occur at the single-particle level, and also at the collective level.

The vertex correction $\Pi_{\bar{\sigma}\sigma}$, Eq. (26), describes the collective propagation of transverse spin density of electrons in a uniform antiferromagnet. The corresponding quantity for a ferromagnet is given by

$$\Pi^{(\mathrm{Ferro})}_{\bar{\sigma}\sigma}(\boldsymbol{q},\omega) = \frac{n_{\mathrm{imp}} u^2_{\mathrm{imp}}}{\left(Dq^2 + 2i\sigma M - i\omega + \tau_{\mathrm{s}}^{-1}\right)\tau}, \tag{44}$$

where M is the coupling to the ferromagnetic moment. The pure-imaginary term $2i\sigma M$ in the denominator of Eq. (44) describes spin precession, but the corresponding term is absent in Eq. (26) for (collinear) antiferromagnets. This means that spin precession is virtually absent in antiferromagnets, and this is reasonable considering the alternating nature of the ordered moments (effective fields). The real term τ_φ^{-1} in the denominator of Eq. (26) describes spin relaxation (dephasing) [14], similar to τ_{s}^{-1} in Eq. (44), but restricted to the transverse components. Here, it arises from *nonmagnetic* impurities. This contrasts with ferromagnets, in which some spin-flip scattering is necessary for spin relaxation to arise. As seen from Eq. (28), τ_φ^{-1} is proportional to γ_3 and J; the former (γ_3) introduces sublattice asymmetry (through $\tau^3\sigma^z$ in self-energy), while the latter (J) represents spin precession with site-to-site alternation. These together violate the above-mentioned cancellation of sublattice-dependent precession and leads to dephasing [6,14].

The vertex correction $\Pi_{\bar{\sigma}\sigma}$, Eq. (26), for antiferromagnets is large in the "weak-AF" regime, $J \ll |\mu|$, where a precise analogy to (ii) for ferromagnets comes up. In this case, $\sigma^{(0)}_{xy}$ is proportional to J^3, as understood perturbatively [20–22], whereas $\sigma^{(\mathrm{VC})}_{xy}$ is linearly proportional to J, a nonperturbative effect due to $\Pi_{\bar{\sigma}\sigma}$. Thus, $\sigma^{(\mathrm{VC})}_{xy}$ dominates $\sigma^{(0)}_{xy}$ by a factor of $\tau_\varphi/\tau \simeq (\mu/J)^2$ (except for a narrow region, $|\mu| \lesssim \sqrt{3}J$; see the curves for $J/t = 0.2$ in Fig. 4), which reflects the behavior of τ_φ; for smaller J, the conduction electrons keep their transverse spin for a longer time, and $\sigma^{(\mathrm{VC})}_{xy}$ is enhanced. As stated above, the same happens in weak-coupling ferromagnets. Note, however, that, in contrast to the ferromagnetic case, the present THC is linear in $\boldsymbol{l}$ regardless of the strength of the exchange coupling constant J.

3. Effective mass dependence at low carrier density

To see the dependence on the effective mass, we consider the regime of low carrier density. When the chemical potential lies near the bottom of the lower AF band (or the top of the upper AF band), the electron dispersion can be approximated by a parabolic one, and η and η' tend to coincide. In fact, if we set $\tilde{\mu} = 1 - \delta\tilde{\mu}$, where $\delta\tilde{\mu}$ measures the distance from the band bottom (or top) and is related to the electron (or hole) number per site n as $\delta\tilde{\mu} = \pi n/2$, one has

$$\eta \simeq \eta' \simeq \frac{J^2(4t)^2}{((4t)^2 + J^2)((4t)^2 + 2J^2)} \frac{\delta\tilde{\mu}}{2\pi} \tag{45}$$

to the leading order in $\delta\tilde{\mu}$. Then, $\frac{\sigma^{(\mathrm{VC})}_{xy}}{\sigma^{(0)}_{xy}} \simeq \frac{\mu^2 - J^2}{4J^2} \simeq \left(\frac{2t}{J}\right)^2$. For $J \lesssim t$ ("weak-AF" regime) [25], the effect of VC is significant. In this case, the THC is inversely proportional to the effective mass, $m^* = \sqrt{(4t)^2 + J^2}/8t^2$, and the TH resistivity is proportional to m^*, $\rho_{xy} \propto m^*$. This feature is shared by ferromagnets in the weak-coupling regime [11].

In the "strong-AF" regime, $J \gtrsim 4t$ [25], the VC is less important. In this case, the THC is independent of the effective mass $m^* \simeq J/8t^2$, and the TH resistivity is proportional to the square of m^*, $\rho_{xy} \propto (m^*)^2$. This result may be relevant to the experiment in Ref. [10].

In Ref. [10], the authors reported a very large TH resistivity ρ_{xy} in Mn oxide thin films at low carrier density n. To interpret their experimental result that ρ_{xy} shows a strong n dependence ($\rho_{xy} \propto n^{-\beta}$ with $\beta \simeq 2.7$), they noted that the weak-coupling formula of ρ_{xy} obtained for ferromagnets [11] is *linearly* proportional to the effective mass m^* (in contrast to the strong-coupling formula, which is independent of m^*), and supposed that m^* would be enhanced at low n like $m^* \propto n^{-\alpha}$ because of some many-body effects not included in the theoretical calculation. To fit the experimental data, they assumed a rather strong n dependence with $\alpha = 2$. With the present result for canted antiferromagnets that ρ_{xy} is proportional to the *square* of m^*, a more moderate behavior with $\alpha = 1$ would be sufficient to fit the data.

B. Examples of spin texture

As shown in Eq. (37), the emergent field that induces THE in antiferromagnets consists of two terms. The first one is due to the spin chirality formed by $\hat{\boldsymbol{l}}$, and the detailed form of $\boldsymbol{n}$ is irrelevant. The second term is associated with the variation of the magnitude $|\boldsymbol{l}|$, and also requires a concert of $\boldsymbol{n}$ and $\boldsymbol{l}$. Here we present an example of spin texture that gives rise to each term in the emergent field.

1. l-skyrmion

If $|\boldsymbol{l}|$ is constant, then the second term vanishes in Eq. (37). The first term is finite when $\boldsymbol{l}$ forms, e.g., a skyrmion ("$\boldsymbol{l}$ skyrmion") as illustrated in Fig. 6(a). In this case, the Néel vector, an example of which is shown in Fig. 6(b), inevitably has singularity (in the bulk) or winding (on the edge) as explained in the caption. Since singularities (vortices in the present case) of the Néel vector are energetically unfavorable, we suppose that, when $\boldsymbol{l}$ forms a skyrmion, $\boldsymbol{n}$ winds twice about the equator along the edge of the system as in Fig. 6(b).

When there are finite density of such $\boldsymbol{l}$ skyrmions, the THC is given by

$$\sigma_{xy} = 4\pi e^2 J|\boldsymbol{l}||\mu|\,\tau^2\left(\eta + \frac{\mu^2 - J^2}{4J^2}\eta'\right)n_{\mathrm{sk}}, \tag{46}$$

where n_{sk} is the sheet (two-dimensional) density of $\boldsymbol{l}$ skyrmions. Here we estimated $\langle B_{\mathrm{s},z}\rangle = 4\pi|\boldsymbol{l}|n_{\mathrm{sk}}$ using the chirality-density formula [the first term of Eq. (37)]. The factor of 4π comes from the solid angle subtended by the $\hat{\boldsymbol{l}}$ vector per skyrmion. Alternatively, the expression $B_{\mathrm{s},z} = (\boldsymbol{\nabla}\times\boldsymbol{A}_{\mathrm{AF}})_z$ [Eq. (34)] allows us to calculate $\langle B_{\mathrm{s},z}\rangle$ purely from the edge spin texture. Focussing on a single skyrmion

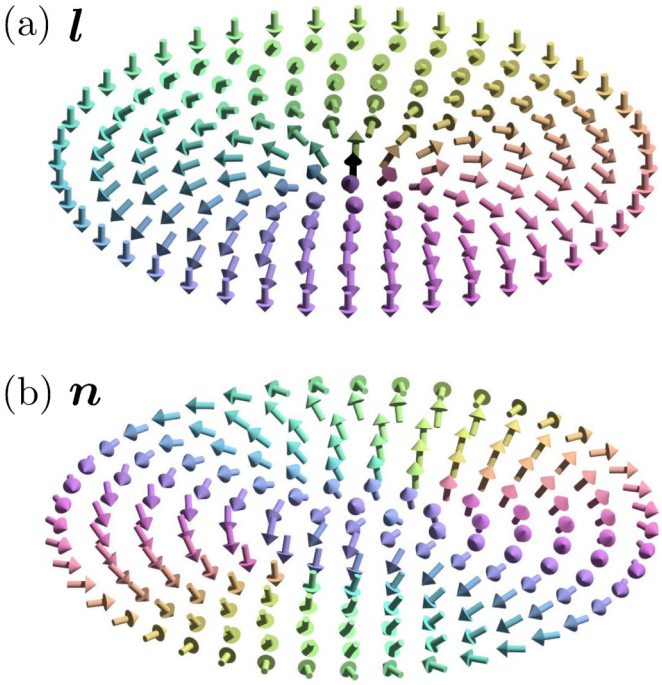

FIG. 6. An example of spin texture that gives rise to the emergent field, $B_{s,z} \sim |\boldsymbol{l}|\hat{\boldsymbol{l}} \cdot (\partial_x \hat{\boldsymbol{l}} \times \partial_y \hat{\boldsymbol{l}})$, the first term of Eq. (37). (a) Uniform component $\boldsymbol{l}$. (b) Néel component $\boldsymbol{n}$. When the uniform component $\hat{\boldsymbol{l}}$ forms a skyrmion, as illustrated in panel (a), the Néel vector $\boldsymbol{n}$, which is locally normal to $\hat{\boldsymbol{l}}$, would form a texture such as the one illustrated in panel (b). Since panel (a) is obtained by a stereographic projection from the normal vector field of a two-sphere (with the direction of vectors preserved), the Néel vector $\boldsymbol{n}$ can be obtained from a tangent vector field by the same projection. Since any tangent vector field on a two-sphere inevitably has singularity (a pole with index 2, or two poles with index 1), known as the "hairy ball theorem" [26], the Néel vector must also form a pole (or poles) of the same character. The only way to avoid the singularity in the Néel vector is to spread the pole to the edge of the system. The Néel vector shown in panel (b) is obtained in this way, and therefore it winds twice the equator as one travels around the edge. (The color of the arrow indicates its in-plane direction.)

for simplicity, we consider

$$\int_S B_{s,z} dxdy = \oint_C A_{\mathrm{AF},i} dx_i = -|\boldsymbol{l}| \oint_C (\partial_i \boldsymbol{n} \times \boldsymbol{n})^z dx_i, \quad (47)$$

where S is the two-dimensional region displayed in Fig. 6, and C is its perimeter. [Note that $\boldsymbol{l} = (0, 0, -|\boldsymbol{l}|)$ on the edge, as seen from Fig. 6(a).] Then, the factor of 4π comes from the in-plane winding angle of the $\boldsymbol{n}$-vector, $\oint_C (\boldsymbol{n} \times \partial_i \boldsymbol{n})^z dx_i = 4\pi$ [see Fig. 6(b)]. Here, in using the Stokes theorem, we assumed that the vector field $\boldsymbol{n}$ has no singularity in S.

A single winding [winding angle by 2π, or precisely, by -2π around $\hat{\boldsymbol{l}} = (0, 0, -1)$] of the in-plane Néel vector $\boldsymbol{n}$ on the perimeter can be absorbed into the bulk as a vortex (not anti-vortex) in which $\boldsymbol{n}$ circulates around $\boldsymbol{l}$ (in the plane perpendicular to $\boldsymbol{l}$). If there are such vortices in the bulk, then the winding angle along the perimeter is reduced, but one has to consider the integration along contours that circle the vortices in the opposite (clockwise) sense, and the total result is the same [27]. Here, we can relax the constraint of constant $|\boldsymbol{l}|$, and evaluate the effective flux as

$$\int_S B_{s,z} dxdy = \oint_{C - \sum_i C_i} A_{\mathrm{AF},i} dx_i = -2\pi \left\{ \oint_C |\boldsymbol{l}| dN_{\mathrm{edge}} - \sum_i N_i |\boldsymbol{l}_i| \right\}, \quad (48)$$

where S now represents the whole sample region with the singularity points excluded, C (C_i) is the contour on the edge (around ith singularity), $\boldsymbol{l}_i = \boldsymbol{l}(\boldsymbol{x}_i)$ is evaluated at the position $\boldsymbol{x}_i$ of ith singularity and $N_i = \frac{1}{2\pi} \oint_{C_i} \hat{\boldsymbol{l}}_i \cdot (\boldsymbol{n} \times \partial_j \boldsymbol{n}) dx_j$ is its vorticity. The winding number along C is given by $N_{\mathrm{edge}} = \oint_C dN_{\mathrm{edge}}$ with the differential, $dN_{\mathrm{edge}} = \frac{1}{2\pi} \hat{\boldsymbol{l}} \cdot (\boldsymbol{n} \times d\boldsymbol{n})$ [28]. If specialized again to the case that $|\boldsymbol{l}|$ is constant, then this reduces to

$$\int_S B_{s,z} dxdy = -2\pi |\boldsymbol{l}| (N_{\mathrm{edge}} - N_{\mathrm{v}}), \quad (49)$$

where $N_{\mathrm{v}} = \sum_i N_i$ is the total vorticity in S. Because of the topological constraint, $N_{\mathrm{v}} - N_{\mathrm{edge}} = 2N_{\mathrm{sk}}$, where N_{sk} is the number of $\boldsymbol{l}$ skyrmions, Eq. (49) leads to $\langle B_{s,z} \rangle = 4\pi |\boldsymbol{l}| n_{\mathrm{sk}}$, and thus to Eq. (46).

2. *n*-domain wall with canting gradient

If the direction of $\boldsymbol{l}$ is constant, then the first term vanishes in Eq. (37). As an example that contributes to the second term in this case, consider a domain wall formed by the Néel vector $\boldsymbol{n}$ lying in the xz plane, $\boldsymbol{n} = [(\cosh \frac{x}{\lambda})^{-1}, 0, \tanh \frac{x}{\lambda}]$, with a uniform component, $\boldsymbol{l} = (0, a + by, 0)$, pointing in the y direction and varying in magnitude in the y direction (λ, a, and b are constants). In this case, $\boldsymbol{A}_{\mathrm{AF}}$ has a nonzero x component, and its cross product with $\nabla |\boldsymbol{l}|$ ($\parallel \hat{y}$) is finite. Such a texture may be realized if a magnetic field gradient is applied on a "Néel-type" AF domain wall (a domain wall formed by $\boldsymbol{n}$ with $\mathrm{div}\boldsymbol{n} \neq 0$) in the direction perpendicular to the Néel vector plane. The degree of canting $|\boldsymbol{l}|$ may also be changed by gradating some material parameters.

To evaluate the THC, let us first look at the effective flux obtained by integrating $B_{s,z} = -b(\lambda \cosh \frac{x}{\lambda})^{-1}$ in a rectangle region, $|x| \leqslant L_x/2$ and $|y| \leqslant L_y/2$ with $L_x \gg \lambda$, which contains a single domain wall (in the x direction),

$$\int_{L_x \times L_y} B_{s,z} dxdy = \int_{-L_x/2}^{L_x/2} \frac{-bL_y}{\lambda \cosh \frac{x}{\lambda}} dx = -\pi b L_y. \quad (50)$$

When there are N_{DW} domain walls in the interval of length L_x, Eq. (50) is multipied by N_{DW}, and we have $\langle B_{s,z} \rangle = -\pi b \rho_{\mathrm{DW}}$, where $\rho_{\mathrm{DW}} = N_{\mathrm{DW}}/L_x$ is the line (one-dimensional) density of the domain walls. This leads to

$$\sigma_{xy} = -\pi e^2 b J |\mu| \tau^2 \left(\eta + \frac{\mu^2 - J^2}{4J^2} \eta' \right) \rho_{\mathrm{DW}}. \quad (51)$$

It should be noted that this holds when all domain walls have the same chirality. When both chiralities, $\boldsymbol{n}_\pm = [\pm(\cosh \frac{x}{\lambda})^{-1}, 0, \tanh \frac{x}{\lambda}]$, coexist, ρ_{DW} is given by $\rho_{\mathrm{DW}} = (N_{\mathrm{DW},+} - N_{\mathrm{DW},-})/L_x$, where $N_{\mathrm{DW},\pm}$ is the number of domain walls of type $\boldsymbol{n}_\pm$.

The above expression can also be obtained from Eq. (48). Since there are no singularities in the bulk, the THC is determined by the winding along the perimeter. For the calculation,

it is sufficient to observe the followings. (i) On the edges perpendicular to the domain walls ($y = \pm L_y/2$), $|\boldsymbol{l}| = |a \pm bL_y/2|$ is constant on each edge, and the respective winding number is $N_{\rm edge} = \pm s_\pm (N_{{\rm DW},+} - N_{{\rm DW},-})/2$ with $s_\pm = {\rm sgn}(a \pm bL_y/2)$. (ii) Along the edges parallel to the domain walls, there is no winding, $dN_{\rm edge} = 0$.

VI. SUMMARY

In this paper, we calculated the topological Hall conductivity in a weakly canted antiferromagnet to the leading order in the spatial gradient of spin texture, uniform moment $\boldsymbol{l}$, and electron damping γ. The uniform moment induced by canting is assumed small and is treated perturbatively. This means that we considered the weak-coupling regime in the sense that $J|\boldsymbol{l}| \ll \gamma$, namely, the spin splitting (due to $\boldsymbol{l}$) is smaller than the broadening in the electron spectrum while the coupling to the AF moment is left arbitrary (thus including both the weak-AF regime and the strong-AF regime). The obtained THC [Eqs. (31)–(33)] is first order in uniform moment $|\boldsymbol{l}|$, second order in scattering time τ, and proportional to an emergent magnetic field [Eq. (37)], which consists of a spin-chirality density formed by the normalized uniform moment $\hat{\boldsymbol{l}}$ and that coming from spatial variation of canting $|\boldsymbol{l}|$.

Whether a given antiferromagnet is in the strong-AF regime or in the weak-AF regime depends on the chemical potential μ relative to the AF band structure. If it is located close to the AF gap edge ($|\mu| \lesssim \sqrt{3}J$), then it is in the strong-AF regime, where the vertex corrections are unimportant and the topological Hall resistivity is proportional to the square of the effective mass, $\rho_{xy} \propto (m^*)^2$. In the weak-AF regime ($|\mu| \gtrsim \sqrt{3}J$), the vertex correction is important, and one sees $\sigma_{xy} \propto J$; this J-linear dependence is a nonperturbative result due to the long dephasing time, $\tau_\varphi \propto J^{-2}$, coming from the vertex correction.

Enhancement due to vertex corrections in the weak-AF regime is also observed in the topological *spin* Hall effect in (locally collinear) antiferromagnets but in a somewhat different way. This will be reported elsewhere [29].

ACKNOWLEDGMENTS

We thank Manuel Bibes for turning our attention to canted antiferromagnets and for enlightening discussions. We also thank T. Funato, Y. Imai, T. Yamaguchi, A. Yamakage, K. Yamamoto, and Y. Yamazaki for helpful discussion. This work is supported by JSPS KAKENHI Grants No. JP15H05702, No. JP17H02929, and No. JP19K03744. J.J.N. is supported by a Program for Leading Graduate Schools "Integrative Graduate Education and Research in Green Natural Sciences" and Grant-in-Aid for JSPS Research Fellow Grant No. 19J23587.

APPENDIX: DERIVATION OF EQ. (37)

Consider an orthonormal frame $\{\hat{\boldsymbol{l}}, \boldsymbol{m}, \boldsymbol{n}\}$ formed by $\boldsymbol{n}$, $\hat{\boldsymbol{l}} \equiv \boldsymbol{l}/|\boldsymbol{l}|$ and $\boldsymbol{m} \equiv \boldsymbol{n} \times \hat{\boldsymbol{l}}$. Using $\boldsymbol{n} = \hat{\boldsymbol{l}} \times \boldsymbol{m}$, and then $\boldsymbol{m} \times \boldsymbol{n} = \hat{\boldsymbol{l}}$, one may calculate as

$$\begin{aligned}
&\partial_y \boldsymbol{n} \cdot (\boldsymbol{n} \times \partial_x \hat{\boldsymbol{l}}) - (x \leftrightarrow y) \\
&= (\partial_y \hat{\boldsymbol{l}} \times \boldsymbol{m} + \hat{\boldsymbol{l}} \times \partial_y \boldsymbol{m}) \cdot (\boldsymbol{n} \times \partial_x \hat{\boldsymbol{l}}) - (x \leftrightarrow y) \\
&= \boldsymbol{m} \times (\boldsymbol{n} \times \partial_x \hat{\boldsymbol{l}}) \cdot \partial_y \hat{\boldsymbol{l}} - (x \leftrightarrow y) \\
&= (\partial_x \hat{\boldsymbol{l}} \cdot \boldsymbol{m})(\partial_y \hat{\boldsymbol{l}} \cdot \boldsymbol{n}) - (\partial_x \hat{\boldsymbol{l}} \cdot \boldsymbol{n})(\partial_y \hat{\boldsymbol{l}} \cdot \boldsymbol{m}) \\
&= (\partial_x \hat{\boldsymbol{l}} \times \partial_y \hat{\boldsymbol{l}}) \cdot \hat{\boldsymbol{l}}. \qquad \text{(A1)}
\end{aligned}$$

In the third line, we noted the orthogonality relations $\boldsymbol{n} \cdot \hat{\boldsymbol{l}} = 0$ and $\hat{\boldsymbol{l}} \cdot \partial_x \hat{\boldsymbol{l}} = 0$. Therefore, $B_{{\rm s},z}$ given by Eq. (35) is expressed as

$$B_{{\rm s},z} = |\boldsymbol{l}|\, \hat{\boldsymbol{l}} \cdot (\partial_x \hat{\boldsymbol{l}} \times \partial_y \hat{\boldsymbol{l}}) + [(\nabla |\boldsymbol{l}|) \times (\boldsymbol{A}_{\rm AF}/|\boldsymbol{l}|)]_z. \qquad \text{(A2)}$$

[1] J. Ye, Y. B. Kim, A. J. Millis, B. I. Shraiman, P. Majumdar, and Z. Tešanović, Phys. Rev. Lett. **83**, 3737 (1999).
[2] P. Bruno, V. K. Dugaev, and M. Taillefumier, Phys. Rev. Lett. **93**, 096806 (2004).
[3] U. K. Rößler, A. N. Bogdanov, and C. Pfleiderer, Nature (London) **442**, 797 (2006).
[4] S. Mühlbauer, B. Binz, F. Jonietz, C. Pfleiderer, A. Rosch, A. Neubauer, R. Georgii, and P. Böni, Science **323**, 915 (2009).
[5] T. Jungwirth, X. Marti, P. Wadley, and J. Wunderlich, Nat. Nanotechnol. **11**, 231 (2016).
[6] V. Baltz, A. Manchon, M. Tsoi, T. Moriyama, T. Ono, and Y. Tserkovnyak, Rev. Mod. Phys. **90**, 015005 (2018).
[7] P. M. Buhl, F. Freimuth, S. Blügel, and Y. Mokrousov, Phys. Status Solidi Rapid Res. Lett. **11**, 1700007 (2017).
[8] B. Göbel, A. Mook, J. Henk, and I. Mertig, Phys. Rev. B **96**, 060406(R) (2017).
[9] C. A. Akosa, O. A. Tretiakov, G. Tatara, and A. Manchon, Phys. Rev. Lett. **121**, 097204 (2018).
[10] L. Vistoli, W. Wang, A. Sander, Q. Zhu, B. Casals, R. Cichelero, A. Barthélémy, S. Fusil, G. Herranz, S. Valencia, R. Abrudan, E. Weschke, K. Nakazawa, H. Kohno, J. Santamaria, W. Wu, V. Garcia, and M. Bibes, Nat. Phys. **15**, 67 (2019).
[11] K. Nakazawa, M. Bibes, and H. Kohno, J. Phys. Soc. Jpn. **87**, 033705 (2018); K. Nakazawa and H. Kohno, Phys. Rev. B **99**, 174425 (2019).
[12] G. Tatara, H. Kohno, and J. Shibata, Phys. Rep. **468**, 213 (2008).
[13] See Supplemental Material at http://link.aps.org/supplemental/10.1103/PhysRevB.101.174432 for details of the calculation (Green's function, vertex correction, topological Hall conductivity, η and η', diagonal conductivity, and density of states) and for some formulas for the discussion on gauge invariance.
[14] A. Manchon, J. Phys.: Condens. Matter **29**, 104002 (2017).
[15] The emergent vector potential $\boldsymbol{A}_{\rm AF}$ should not be confused with the spin gauge field introduced in Eq. (6); the latter is related solely to the Néel vector and has a gauge degree of freedom (rotation around $\boldsymbol{n}$). The vector potential $\boldsymbol{A}_{\rm AF}$ here depends on $\boldsymbol{l}$ as well, and it is uniquely determined by the physical fields, $\boldsymbol{n}$ and $\boldsymbol{l}$, and has no gauge degree of freedom.
[16] F. D. M. Haldane, Phys. Rev. Lett. **50**, 1153 (1983).
[17] B. A. Ivanov and A. K. Kolezhuk, Phys. Rev. Lett. **74**, 1859 (1995).
[18] E. G. Tveten, T. Müller, J. Linder, and A. Brataas, Phys. Rev. B **93**, 104408 (2016).

[19] Y. Toda, Master thesis (Nagoya University, March 2017).
[20] G. Tatara and H. Kawamura, J. Phys. Soc. Jpn. **71**, 2613 (2002).
[21] K. Nakazawa and H. Kohno, J. Phys. Soc. Jpn. **83**, 073707 (2014).
[22] K. S. Denisov, I. V. Rozhansky, N. S. Averkiev, and E. Lähderanta, Phys. Rev. Lett. **117**, 027202 (2016).
[23] J. Shibata and H. Kohno, Phys. Rev. B **84**, 184408 (2011).
[24] H. Kohno and J. Shibata, J. Phys. Soc. Jpn. **76**, 063710 (2007).
[25] As described near the end of Sec. IV, the weak- (strong-) AF regime is defined by $|\mu| \gtrsim \sqrt{3}J$ ($|\mu| \lesssim \sqrt{3}J$). At low carrier density, where $|\mu| \sim \sqrt{(4t)^2 + J^2}$, this condition is equivalent to $\sqrt{3}J \lesssim 4t$ ($\sqrt{3}J \gtrsim 4t$). Note that for $J \gg 4t$ the whole band (whole μ region) is in the strong-AF regime.
[26] M. Eisenberg and R. Guy, Am. Math. Mon. **86**, 571 (1979).
[27] The integration in the negative (clockwise) sense along the encircling countour gives -2π per vortex.
[28] As this differential expression suggests, the integration can also be taken on the corresponding contour on the unit sphere used in the stereographic projection (see the caption of Fig. 6). This is so because $dx_i\partial_i$ is invariant under general coordinate transformations. Then, on the unit sphere, the contour C encircles the south pole, whereas C_i's do not. This offers a simpler picture for the topological consideration, such as the topological constraint, $N_{\rm v} - N_{\rm edge} = 2N_{\rm sk}$, given below.
[29] K. Nakazawa *et al.* (unpublished).